Halo modelling in chameleon theories

Lucas Lombriser,[a,b] **Kazuya Koyama,**[a] **Baojiu Li**[c]

[a]Institute of Cosmology and Gravitation, University of Portsmouth, Dennis Sciama Building, Burnaby Road, Portsmouth, PO1 3FX, U.K.

[b]Institute for Astronomy, University of Edinburgh, Royal Observatory, Blackford Hill, Edinburgh, EH9 3HJ, U.K.

[c]Institute for Computational Cosmology, Ogden Centre for Fundamental Physics, Department of Physics, University of Durham, Science Laboratories, South Road, Durham, DH1 3LE, U.K.

E-mail: lucas.lombriser@port.ac.uk, kazuya.koyama@port.ac.uk, baojiu.li@durham.ac.uk

Abstract. We analyse modelling techniques for the large-scale structure formed in scalar-tensor theories of constant Brans-Dicke parameter which match the concordance model background expansion history and produce a chameleon suppression of the gravitational modification in high-density regions. Thereby, we use a mass and environment dependent chameleon spherical collapse model, the Sheth-Tormen halo mass function and linear halo bias, the Navarro-Frenk-White halo density profile, and the halo model. Furthermore, using the spherical collapse model, we extrapolate a chameleon mass-concentration scaling relation from a ΛCDM prescription calibrated to N-body simulations. We also provide constraints on the model parameters to ensure viability on local scales. We test our description of the halo mass function and nonlinear matter power spectrum against the respective observables extracted from large-volume and high-resolution N-body simulations in the limiting case of $f(R)$ gravity, corresponding to a vanishing Brans-Dicke parameter. We find good agreement between the two; the halo model provides a good qualitative description of the shape of the relative enhancement of the $f(R)$ matter power spectrum with respect to ΛCDM caused by the extra attractive gravitational force but fails to recover the correct amplitude. Introducing an effective linear power spectrum in the computation of the two-halo term to account for an underestimation of the chameleon suppression at intermediate scales in our approach, we accurately reproduce the measurements from the N-body simulations.

arXiv:1312.1292v1 [astro-ph.CO] 4 Dec 2013

Contents

1   Introduction

In the effective field theory limit at low energies, models attempting to unify general relativity with the standard model interactions are typically expected to introduce a scalar field in addition to the gravitational tensor field, which may couple minimally or nonminimally to the matter fields. This fifth element can source the observed late-time acceleration of our Universe as an alternative to the cosmological constant (cf. [1]). A nonminimal coupling consequently leads to a modification of the gravitational interactions between the matter fields, which is, however, tightly constrained by local observations [2]. If the scalar field potential has an adequate form, it can contribute to alleviate these constraints such as is the case in chameleon models [3–6], where the curvature dependence of the scalar field is such to suppress the extra force in high-density regions. At low curvature and below the Compton wavelength of the scalar field, the gravitational force remains enhanced, yielding an increase in the growth of structure.

Here, we specialise to scalar-tensor models with constant Brans-Dicke parameter ω that match the ΛCDM background expansion history, exhibit a chameleon mechanism, and reduce to the Hu-Sawicki [7] $f(R)$ model [8–13] in the limit of $\omega = 0$. The enhanced gravitational coupling of these models at low curvature and below the Compton wavelength can be utilised to place observational constraints on the gravitational modifications. Such constraints from current and expected from future observations have been particularly well studied in the limiting case of $f(R)$ gravity [7, 14–55]. Currently, the strongest bounds on these modifications

are inferred from the transition required to interpolate between the low curvature of the large-scale structure and the high curvature of the galactic halo [7] as well as from the comparison of nearby distance measurements in a sample of unscreened dwarf galaxies [36]. Hereby, in order to guarantee chameleon screening, the background field amplitude has to be smaller than the corresponding depth of the potential wells, $|\Psi| \sim (10^{-7} - 10^{-5})$. Independently, strong observational constraints have also been inferred from the large-scale structure such as from the analysis of cluster profiles [56] and abundance [22, 25, 28], which are however, still 2-3 orders of magnitude weaker than the bounds inferred from the local and astrophysical tests. Note, however, that while astrophysical and Solar System tests require the chameleon field to couple to the baryonic components, due to the dominance of the dark matter on cosmological scales, probes of the large-scale structure are typically independent of this assumption. Such dark chameleon fields that only couple to dark matter may furthermore evade problems arising in the early universe due to high-energy fluctuations through quantum particle production [57, 58]. The current cosmological bounds have been obtained from an analysis of massive clusters, implying constraints that lie in a regime where the modified observables can correctly be described by performing a linearisation of the scalar field potential. This approach breaks down for clusters with gravitational potential wells of the order of $|\Psi| \lesssim 10^{-5}$, for which the chameleon mechanism becomes important and needs to be incorporated correctly.

While N-body simulations of such scalar-tensor theories provide a great laboratory for studying the chameleon mechanism [59–64], they are computationally expensive and more efficient modelling of the large-scale structure needs to be developed based on these simulations in order to allow for a full exploration of the cosmological parameter space in the model comparison to observations. In this paper, we provide simple modelling techniques for the large-scale structure produced in chameleon theories, providing an important tool for efficiently extrapolating and interpolating the nonlinear quantities extracted from N-body simulations beyond the simulated values of the cosmological and chameleon model parameters implemented. These tools are essential to allow the consistent inference of model constraints from the observed large-scale structure, enabling sufficient and smooth variation of chain parameters as well as statistical convergence.

In Sec. 2, we give a short review on scalar-tensor theories with a particular focus on chameleon models. We generalise the Hu-Sawicki $f(R)$ chameleon model to scalar-tensor theories with constant Brans-Dicke parameter and discuss the background and Solar System constraints on these models. In Sec. 3, we describe the formation of large-scale structure in chameleon models using linear cosmological perturbation theory in the quasistatic limit, the mass and environment dependent spherical collapse model [65], methods for environmental averaging, and dark matter N-body simulations. In Sec. 4, we describe the halo model for chameleon theories and analyse its performance against N-body simulations in the limiting case of $f(R)$ gravity. In specific, we follow the computation of Ref. [66] and use the Sheth-Tormen prescription [67] to obtain the halo mass function and extend this approach to the description of the linear halo bias. Based on the chameleon spherical collapse model, we introduce a chameleon transition in the scaling of concentration with respect to mass and use this to describe the halo density profile assuming a Navarro-Frenk-White (NFW) [68] profile, which has been shown to provide good fits to chameleon halos in the limit of $f(R)$ gravity [56]. Combining these quantities in the halo model, we compute the nonlinear matter power spectrum for chameleon theories. We test our description against dark matter N-body simulations of chameleon $f(R)$ gravity models, finding good agreement between the two; the halo model provides a good qualitative description of the chameleon suppression in the

nonlinear matter power spectrum but fails to reproduce the correct amplitude of the relative enhancement due to the chameleon field. By introducing a transition between the linear $f(R)$ and ΛCDM power spectrum in the two-halo term to account for an underestimation of the chameleon suppression on intermediate scales, we improve the halo model description to obtain an accurate fit to the nonlinear matter power spectrum extracted from N-body simulations over a wide range of scales. Finally, in Sec. 5, we conclude with a discussion of our results.

2 Chameleon model

We consider scalar-tensor theories for which the modified Einstein-Hilbert action in the Jordan frame can be written in the form

$$S = \frac{1}{2\kappa^2} \int d^4x \sqrt{-g}\left[F(\varphi)R - Z(\varphi)\partial^\mu\varphi\,\partial_\mu\varphi - 2U(\varphi)\right] + S_{\rm m}[\psi_{\rm m}; g_{\mu\nu}], \tag{2.1}$$

where $\kappa^2 \equiv 8\pi\,G$ with the bare gravitational coupling G, R is the Ricci scalar, $S_{\rm m}$ is the matter action with matter fields $\psi_{\rm m}$, and we have set the speed of light in vacuum to unity. The scalar field φ is coupled to the metric $g_{\mu\nu}$ via $F(\varphi)$ with kinetic coupling $Z(\varphi)$ and scalar field potential $U(\varphi)$. It can be redefined to reduce the number of free functions of φ in Eq. (2.1) to two instead of three. In this paper, we will use the Brans-Dicke [69] representation for scalar-tensor models,

$$F \equiv \varphi, \qquad Z \equiv \frac{\omega(\varphi)}{\varphi}. \tag{2.2}$$

We can recast the Jordan frame action Eq. (2.1) into the Einstein frame by a conformal transformation of the metric such that

$$S = \int d^4x \sqrt{-\tilde{g}}\left[\frac{\tilde{R}}{2\kappa^2} - \frac{1}{2}\tilde{\partial}^\mu\phi\,\tilde{\partial}_\mu\phi - V(\phi)\right] + S_{\rm m}[\psi_{\rm m}; A^2(\phi)\tilde{g}_{\mu\nu}], \tag{2.3}$$

where here and throughout the paper, tildes denote quantities in the Einstein frame, and

$$\tilde{g}_{\mu\nu} \equiv \varphi\,g_{\mu\nu}, \tag{2.4}$$

$$\left(\frac{{\rm d}\phi}{{\rm d}\varphi}\right)^2 \equiv \frac{1}{2\kappa^2}\frac{3+2\omega}{\varphi^2}, \tag{2.5}$$

$$A(\phi) \equiv \varphi^{-1/2}, \tag{2.6}$$

$$V(\phi) \equiv \frac{U(\varphi)}{\kappa^2\varphi^2}. \tag{2.7}$$

Integration of Eq. (2.5) relates the Einstein frame to the Jordan frame scalar field,

$$\phi = \frac{1}{\kappa}\sqrt{\frac{3+2\omega}{2}}\ln\varphi + \phi_0, \tag{2.8}$$

where we restricted to cases with Brans-Dicke parameter $\omega = {\rm const.}$ and set $\phi_0 \equiv 0$. This shall also be adopted in the following discussion along with the condition that $\omega > -3/2$ to evade ghost fields. Variation of the action Eq. (2.3) with respect to ϕ yields the scalar field equation

$$\tilde{\Box}\phi = \frac{\kappa}{\sqrt{6+4\omega}}\tilde{T} + V'(\phi) \equiv V'_{\rm eff}(\phi), \tag{2.9}$$

where $V_{\text{eff}}(\phi)$ is an effective potential governing the dynamics of ϕ and the energy-momentum tensor is given by $\tilde{T} = A(\phi)^4 T$. For a scalar field with $\varphi \simeq 1$ minimising the effective potential, $V'_{\text{eff}}(\phi) = 0$, Eq. (2.9) becomes

$$\frac{\mathrm{d}}{\mathrm{d}\varphi} U(\varphi) \simeq \frac{1}{2}(\kappa^2 \rho_{\text{m}} + 4U) \simeq \frac{\tilde{R}}{2} \simeq \frac{R}{2}, \tag{2.10}$$

where we have assumed dominance of the matter energy density ρ_{m} and further required $(\kappa^2 \rho_{\text{m}} + 4U) \gg (3 + 2\omega)(\partial_\mu \varphi)^2 / 2$.

2.1 Background expansion history

We are interested in scalar-tensor theories that predict a background expansion history that closely matches the one of ΛCDM. Combining the Jordan frame scalar field equation and Einstein equations in the background, we obtain the Friedmann equations

$$3\bar{\varphi} H^2 - \kappa^2 \bar{\rho}_{\text{m}} - \frac{H^2}{2} \frac{\omega}{\bar{\varphi}} \bar{\varphi}'^2 + 3H^2 \bar{\varphi}' - \bar{U} = 0, \tag{2.11}$$

$$\omega H^2 \bar{\varphi}'' + H^2 \left[\omega \left(\frac{H'}{H} + 3 \right) - 3 \right] \bar{\varphi}' - 3H^2 \left[\frac{H'}{H} + 3 \right] \bar{\varphi} + \kappa^2 \bar{\rho}_{\text{m}} + \bar{U} + \bar{\varphi} \frac{\mathrm{d}\bar{U}}{\mathrm{d}\bar{\varphi}} = 0, \tag{2.12}$$

where here and throughout the paper, primes denote derivatives with respect to $\ln a$ and overbars refer to quantities evaluated at their background. For $\bar{\varphi} \simeq 1$ and $|\omega^j \bar{\varphi}^{(i)}| \ll 1$ with order of the derivative $i = 1, 2$ and exponent $j = 0, 1$, we can neglect these derivative terms of the scalar field in Eqs. (2.11) and (2.12), and it then follows directly that $\bar{U}_{\bar{\varphi}} \simeq \bar{R}/2$. For $|\bar{\varphi}^{(i)}| \sim |\bar{\varphi} - 1|$, $|\omega| \ll |\bar{\varphi}_0 - 1|^{-1}$, and $\bar{U} \simeq \Lambda$, H^2 is described by a ΛCDM expansion history at order $\mathcal{O}(|\bar{\varphi} - 1|)$.

2.2 Chameleon regime

In high-density regions, where $\kappa \rho_{\text{m}} \gg -\sqrt{6 + 4\omega} \tilde{\nabla}^2 \phi$ in the quasistatic limit, Eq. (2.9) implies that the scalar field potential satisfies $U_\varphi \simeq R/2$ as in Eq. (2.10). We make the ansatz $U = \Lambda + U_\alpha(1 - \varphi)^\alpha$ with positive constant α such that we recover ΛCDM in the limit of $\varphi = 1$. With the requirement that $U_\varphi \simeq R/2$, hence $\alpha \neq 1$, we obtain

$$U \simeq \Lambda - \frac{\bar{R}_0}{2\alpha} \frac{(1 - \varphi)^\alpha}{(1 - \bar{\varphi}_0)^{\alpha-1}} \simeq \Lambda + \frac{\bar{\varphi}_0 - 1}{2\alpha} \left(\frac{\bar{R}_0}{R^\alpha} \right)^{1/(1-\alpha)}, \tag{2.13}$$

$$\varphi \simeq 1 + (\bar{\varphi}_0 - 1) \left(\frac{\bar{R}_0}{R} \right)^{1/(1-\alpha)}, \tag{2.14}$$

where here and throughout the paper, subscripts of zero refer to present time, $a \equiv 1$. Since in high-density regions, $R \gg \bar{R}_0$, for $\alpha < 1$, we get $(\varphi - 1) \simeq 2\kappa/\sqrt{6 + 4\omega} \, \phi \simeq 0$. Consequently, modifications of gravity are suppressed. We further require $\alpha \gg |\bar{\varphi}_0 - 1|$ such that $\bar{U} \simeq \Lambda$ at the background and $|\omega^j||1 - \bar{\varphi}_0| \ll (1 - \alpha)^2$ such that $|\omega^j \varphi^{(i)}| \ll 1$. This satisfies the conditions for φ imposed in Sec. 2.1.

Note that we can alternatively write the scalar field Eq. (2.14) and its potential Eq. (2.13) replacing R with $-\kappa^2 T_{\text{eff}} \simeq (-\kappa^2 T + 4\Lambda) \simeq (\kappa^2 \rho_{\text{m}} + 4\Lambda)$ or $3(H^2 + \Lambda)$ at the background, where T_{eff} is an effective energy-momentum tensor including the dark energy contributions. Furthermore, in the limit of $\omega \equiv 0$, defining $\varphi \equiv 1 + \mathrm{d}f/\mathrm{d}R \equiv 1 + f_R$, the action Eq. (2.1) in the parametrisation Eq. (2.2) and with scalar field potential Eq. (2.13) reduces to the Hu-Sawicki $f(R)$ gravity model [7] with $\alpha \equiv n/(n+1)$. Hence, Eq. (2.13) shall serve here as a straightforward generalisation thereof with model parameters $|\bar{\varphi}_0 - 1|$, ω, and α.

2.3 Linearised regime

In the following, we focus on the quasistatic limit, require $\varphi \simeq 1$, and linearise the contribution of φ to the scalar field potential in Eq. (2.9) with respect to the background. Subsequently subtracting the background, we obtain

$$\tilde{\nabla}^2 \delta\varphi_{\mathrm{lin}} - m^2 \delta\varphi_{\mathrm{lin}} + \frac{\kappa^2}{3+2\omega} \delta\rho_{\mathrm{m}} \simeq 0, \tag{2.15}$$

where we have defined

$$m^2 \equiv \frac{1-\alpha}{3+2\omega} \frac{(1-\bar{\varphi})^{\alpha-2}}{(1-\bar{\varphi}_0)^{\alpha-1}} \bar{R}_0 \simeq \frac{1-\alpha}{3+2\omega} \frac{(\bar{R}_0 \bar{R}^{\alpha-2})^{1/(\alpha-1)}}{1-\bar{\varphi}_0}, \tag{2.16}$$

as well as $\delta\varphi \equiv \varphi - \bar{\varphi}$ and $\delta\rho_{\mathrm{m}} \equiv \rho_{\mathrm{m}} - \bar{\rho}_{\mathrm{m}}$.

In Sec. 3, we will be interested in the large-scale structure formed in chameleon theories. Dark matter halos extracted from ΛCDM N-body simulations are well described assuming sphericity of the halos and that their density profiles are given by the NFW [68] expression

$$\delta\rho_{\mathrm{m}}(r) = \frac{\rho_{\mathrm{s}}}{\frac{r}{r_{\mathrm{s}}}\left(1+\frac{r}{r_{\mathrm{s}}}\right)^2}, \tag{2.17}$$

where ρ_{s} and r_{s} are the characteristic density and scale, respectively, which are fitted to the simulations. It has been shown in Ref. [56] that the NFW fit also correctly describes the dark matter halo density profiles produced in N-body simulations of chameleon $f(R)$ gravity. Motivated by these results, we assume here that it also provides a good description for halo density profiles formed in more general chameleon models defined by the action Eq. (2.1) and the scalar field potential Eq. (2.13). Following the derivation of Ref. [56] under this assumption, the linearised scalar field in the virialised halo is then determined by

$$\delta\varphi_{\mathrm{lin}} \simeq -\frac{\kappa^2 \rho_{\mathrm{s}} r_{\mathrm{s}}^3}{6+4\omega} \left\{ \Gamma[0, m(r+r_{\mathrm{s}})]e^{2m(r+r_{\mathrm{s}})} + \Gamma[0, -m(r+r_{\mathrm{s}})] \right.$$
$$\left. -\Gamma(0, -m\,r_{\mathrm{s}}) - e^{2m\,r_{\mathrm{s}}}\Gamma(0, m\,r_{\mathrm{s}}) \right\} \frac{e^{-m(r+r_{\mathrm{s}})}}{r}, \tag{2.18}$$

where

$$\Gamma(s, r) = \int_r^\infty \mathrm{d}t\, t^{s-1} e^{-t} \tag{2.19}$$

is the upper incomplete gamma function. In the limit of $\rho_{\mathrm{m}} \gg \bar{\rho}_{\mathrm{m}}$, the linearised scalar field becomes

$$\delta\varphi_{\mathrm{lin}} \simeq \frac{\kappa^2 \rho_{\mathrm{s}} r_{\mathrm{s}}^3}{3+2\omega} \left[\frac{\ln(1+r/r_{\mathrm{s}})}{r} - m\,e^{m\,r_{\mathrm{s}}}\Gamma(0, m\,r_{\mathrm{s}}) \right]. \tag{2.20}$$

2.4 Intermediate regime

In Sec. 2.2, we have described the chameleon screening of the scalar field in high-density regions and in Sec. 2.3, the linearised limit of the scalar field when deviations from the background are small. Next, we are interested in the description of the radial profile of the scalar field φ in the intermediate regime, interpolating between the linearised and screened chameleon limits.

We begin by studying the case of a constant spherically symmetric top-hat matter density ρ_{in} of radius r_{th}, embedded in an outer matter density ρ_{out}. On the inside and outside of r_{th},

the effective Einstein frame scalar field potential $V_{\text{eff}}(\phi)$ in Eq. (2.9) is minimised and we refer to the corresponding Jordan frame scalar field as φ_{in} and φ_{out}, respectively. The distance $\Delta r \geq 0$ that is necessary for $\varphi \simeq 1$ to settle from φ_{out} to φ_{in} can be approximated by [4]

$$\frac{\Delta r}{r_{\text{th}}} \simeq (3 + 2\omega)\frac{\varphi_{\text{in}} - \varphi_{\text{out}}}{6\Psi_{\text{N}}} = (3 + 2\omega)\frac{\varphi_{\text{in}} - \varphi_{\text{out}}}{\kappa^2 \rho_{\text{in}} r_{\text{th}}^2}, \tag{2.21}$$

where we have used the Newtonian potential at the surface of the sphere,

$$\Psi_{\text{N}} = \frac{\kappa^2}{8\pi}\frac{M}{r_{\text{th}}} = \frac{\kappa^2}{6}\rho_{\text{in}} r_{\text{th}}^2 \tag{2.22}$$

with mass $M \equiv 4\pi \rho_{\text{in}} r_{\text{th}}^3$. The inner and outer solutions for φ are obtained from $U_\varphi \simeq R/2$ as described in Eq. (2.14) for the chameleon models of interest here. Hence, we have

$$\varphi_{\text{in/out}} \simeq 1 + (\bar{\varphi}_0 - 1)\left[\frac{1 + 4\frac{\Omega_\Lambda}{\Omega_{\text{m}}}}{\tilde{\rho}_{\text{in/out}}a^{-3} + 4\frac{\Omega_\Lambda}{\Omega_{\text{m}}}}\right]^{1/(1-\alpha)}, \tag{2.23}$$

where $\tilde{\rho}_{\text{in/out}} \equiv \rho_{\text{m,in/out}}(a = 1)/\bar{\rho}_{\text{m}}(a = 1)$, such that

$$\frac{\Delta r}{r_{\text{th}}} \simeq \frac{(3 + 2\omega)(\bar{\varphi}_0 - 1)a^3}{3\Omega_{\text{m}}\tilde{\rho}_{\text{in}}(H_0 r_{\text{th}})^2}\left[\left(\frac{1 + 4\frac{\Omega_\Lambda}{\Omega_{\text{m}}}}{\tilde{\rho}_{\text{in}}a^{-3} + 4\frac{\Omega_\Lambda}{\Omega_{\text{m}}}}\right)^{\frac{1}{1-\alpha}} - \left(\frac{1 + 4\frac{\Omega_\Lambda}{\Omega_{\text{m}}}}{\tilde{\rho}_{\text{out}}a^{-3} + 4\frac{\Omega_\Lambda}{\Omega_{\text{m}}}}\right)^{\frac{1}{1-\alpha}}\right]. \tag{2.24}$$

For a thin shell, $\Delta r = r_{\text{th}} - r_0 \ll r_{\text{th}}$, the intermediate scalar field within $r \in [r_0, r_{\text{th}}]$ is described via [4, 65, 66]

$$\varphi(r) \simeq \varphi_{\text{in}} - \frac{1}{3 + 2\omega}\frac{\kappa^2 \rho_{\text{in}}}{3}\left(\frac{r^2}{2} + \frac{r_0^3}{r} - \frac{3}{2}r_0^2\right), \tag{2.25}$$

for which the force enhancement $\Delta F \equiv F - F_{\text{N}}$ at r_{th} with total force F, Newtonian force $F_{\text{N}} = G\, m\, M/r_{\text{th}}^2$, and test mass m_{t} due to the extra coupling becomes

$$\frac{\Delta F}{F_{\text{N}}} \equiv -\frac{m_{\text{t}}}{2F_{\text{N}}}\tilde{\nabla}\varphi\bigg|_{r_{\text{th}}} \simeq \frac{1}{3 + 2\omega}\left[1 - \left(\frac{r_0}{r_{\text{th}}}\right)^3\right]$$

$$= \frac{1}{3 + 2\omega}\left[3\frac{\Delta r}{r_{\text{th}}} - 3\left(\frac{\Delta r}{r_{\text{th}}}\right)^2 + \left(\frac{\Delta r}{r_{\text{th}}}\right)^3\right]. \tag{2.26}$$

As for $r_0 \ll r_{\text{th}}$, we reproduce the force enhancement in the thick-shell regime $\Delta r > r_{\text{th}}$ [65, 66], we apply Eq. (2.26) to all Δr. Hence, we get

$$\frac{\Delta F}{F_{\text{N}}} \simeq \frac{1}{3 + 2\omega}\min\left[3\frac{\Delta r}{r_{\text{th}}} - 3\left(\frac{\Delta r}{r_{\text{th}}}\right)^2 + \left(\frac{\Delta r}{r_{\text{th}}}\right)^3, 1\right], \tag{2.27}$$

yielding an interpolation between the suppressed regime $\Delta F = 0$ and the $\Delta F/F_{\text{N}} = (3+2\omega)^{-1}$ enhancement, which is $\mathcal{C}^0$ for $\Delta r/r_{\text{th}} \to 0$ and $\mathcal{C}^2$ for $\Delta r/r_{\text{th}} \to 1$.

We will use the force enhancement Eq. (2.26) in the spherical collapse model when studying the formation of structure in chameleon theories assuming that dark matter halos are top hats. We can, however, model the scalar field within dark matter halos more accurately

by assuming a fit of the halo density profile as we have done in Sec. 2.3, where we considered the linearised scalar field $\delta\varphi_{\mathrm{lin}}$ within a virialised cluster. Assuming spherical symmetry in the quasistatic limit of the scalar field equation, Eq. (2.9), and that $\delta\rho_{\mathrm{m}}$ is given by a NFW profile, one obtains a second-order differential equation, which can easily be integrated numerically using the substitution $\varphi - 1 = -e^{u(r)}$ (see, e.g., [56, 59, 70]). Alternatively, the chameleon transition can be modelled following the semi-analytic approach of Pourhasan *et al.* [71] for describing the chameleon field by matching the chameleon interior solution of Sec. 2.2, applying to $r \in (r_-, r_+)$, to the chameleon exterior solution of Sec. 2.3 for $r > r_{\mathrm{cham}}$ at the transition scale r_{cham}. More precisely, the integration constants obtained from the integration of the quasistatic scalar field equation in the limit of $\rho_{\mathrm{m}} \gg \bar{\rho}_{\mathrm{m}}$, i.e., when the term $-m^2\delta\varphi$ can be neglected in Eq. (2.15), are defined by matching φ at the background and requiring that the matched scalar field and its derivative are continuous at the transition:

$$\delta\varphi(r) \equiv \left(\delta\varphi^{\mathrm{in}}_{r<r_{\mathrm{cham}}} \cup \delta\varphi^{\mathrm{out}}_{r\geq r_{\mathrm{cham}}}\right)(r) \in \mathcal{C}^1(U) \tag{2.28}$$

with $r_{\mathrm{cham}} \in U \subset \mathbb{R}_0^+$. The transition scale r_{cham} is then computed numerically. Finally, we can also assume an instantaneous transition to $\delta\varphi = 1 - \bar{\varphi}$ simply implemented via [56]

$$\varphi \approx \min\left(\varphi_{\mathrm{lin}}, 1\right) \tag{2.29}$$

or equivalently, $\delta\varphi \approx \min\left(\delta\varphi_{\mathrm{lin}}, 1 - \bar{\varphi}\right)$, using the linearised scalar field φ_{lin} described in Sec. 2.3. All of these approaches have been shown to provide good agreement with N-body simulations of chameleon $f(R)$ gravity [56]. It is important to note, however, that matching $\delta\varphi$ to boundary values such as $\delta\varphi(r_{\mathrm{vir}})$, where r_{vir} is the virial radius, given from simulations is essential for recovering the radial profile of the simulated scalar field.

Using the approximation of an instantaneous chameleon transition Eq. (2.29) in the limit $\rho_{\mathrm{m}} \gg \bar{\rho}_{\mathrm{m}}$, where $\delta\varphi_{\mathrm{lin}}$ is described by Eq. (2.20), the scale of the chameleon transition r_{cham} can be estimated by solving $\delta\varphi_{\mathrm{lin}}(r_{\mathrm{cham}}) \approx 1 - \bar{\varphi}$, which yields

$$r_{\mathrm{cham}} \simeq -r_{\mathrm{s}} - A^{-1}W\left[-A\,r_{\mathrm{s}}\exp(-A\,r_{\mathrm{s}})\right], \tag{2.30}$$

where $W[\cdot]$ is the Lambert W function solving $x = W(x)\exp[W(x)]$ and we have defined

$$A \equiv \frac{3 + 2\omega}{\kappa^2\rho_{\mathrm{s}}r_{\mathrm{s}}^3}(1 - \bar{\varphi}) + m\,e^{m\,r_{\mathrm{s}}}\Gamma(0, m\,r_{\mathrm{s}}). \tag{2.31}$$

2.5 Solar System constraints

Before continuing with the discussion of the formation of structure within chameleon theories in Sec. 3, we provide a short and simplified analysis of the requirements on our chameleon models given through Eqs. (2.1) and (2.13) to be viable within the Solar System. Using the modelling of the scalar field within a dark matter halo described in Sec. 2.4, we estimate Solar System constraints on the model parameter $|1 - \bar{\varphi}_0|$ as a function of ω and α. Hereby, in order to satisfy the tight local constraints on deviations from general relativity [2], we simply require that the Milky Way halo with mass $M_{\mathrm{MW}} \approx 1.26 \times 10^{12}\,M_\odot$ [72] is screened within $r_{\mathrm{cham}} \approx 8$ kpc, where the Solar System is approximately located.

Note that we conservatively assume that the measured value of M_{MW} also applies to the case of modified gravity. As in viable scalar-tensor theories, due to the enhanced gravitational force comparable to Eq. (2.27), dynamically inferred masses are larger than lensing masses, which we use to determine the chameleon screening, the true halo mass can only be smaller
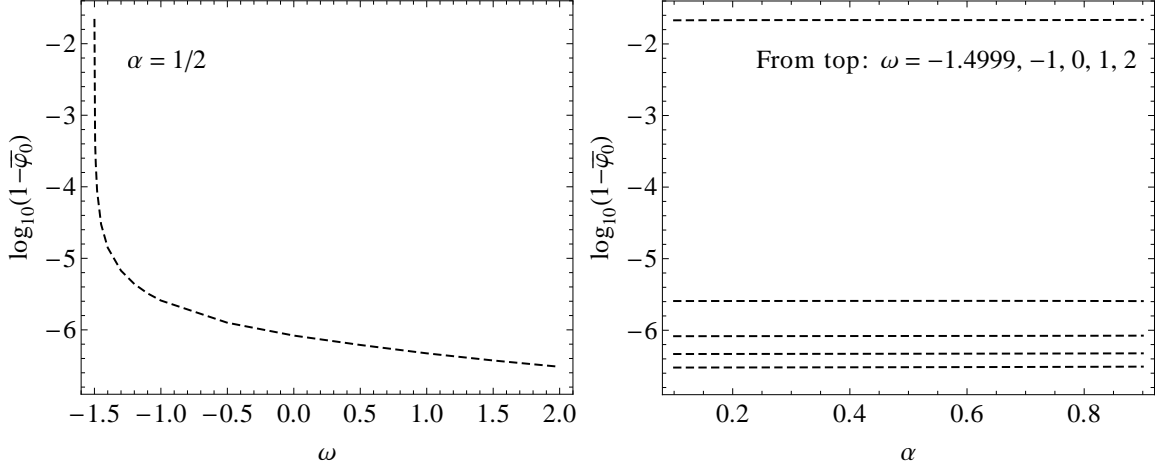
Figure 1. Upper bounds on $\log_{10}(1 - \bar{\varphi}_0)$ ensuring that the chameleon mechanism screens the Solar System from modifications of gravity. Hereby, $\bar{\varphi}_0$ denotes the present cosmological background value of the scalar field. *Left panel:* The constraint depends on the Brans-Dicke parameter ω, which is assumed constant. *Right panel:* Variation of α, which enters the scalar field potential through $|U - \Lambda| \sim |\varphi - 1|^\alpha$, only affects the constraints very weakly through the scalar field mass m, Eq. (2.16), in Eq. (2.31).

than $M_{\rm MW}$, implying stronger constraints on $|\bar{\varphi}_0 - 1|$ in order to achieve screening at the Solar System scale. Hence, using the Milky Way mass inferred assuming general relativity weakens the constraint on $|\bar{\varphi}_0 - 1|$.

For simplicity, we furthermore neglect the bulge and disc and assume that the NFW profile describes the dark matter profile of the Milky Way halo and galaxy sufficiently well for our approximations as well as that the environment can be approximated by the cosmological background. Note that at the scale of the Solar System, the baryonic components dominate over the dark matter and that the inclusion of the baryonic distribution may alleviate constraints on the chameleon field amplitude. As we are only interested in an approximative bound, we choose to neglect the baryonic contribution and leave a more accurate derivation of the Solar System constraints for future work. We model the NFW parameters in Eq. (2.17) via the relations

$$\rho_{\rm s} = \frac{1}{3}\bar{\rho}_{\rm m}\Delta_{\rm vir}c_{\rm vir}^3 \left[\ln(1 + c_{\rm vir}) - \frac{c_{\rm vir}}{c_{\rm vir} + 1}\right]^{-1}, \tag{2.32}$$

$$r_{\rm s} = \frac{1}{c_{\rm vir}}\left(\frac{3M_{\rm vir}}{4\pi\bar{\rho}_{\rm m}\Delta_{\rm vir}}\right)^{1/3}, \tag{2.33}$$

where $c_{\rm vir} \equiv r_{\rm vir}/r_{\rm s}$ is the virial halo concentration, $\Delta_{\rm vir}$ is the virial overdensity, and $M_{\rm vir}$ is the virial halo mass. We assume the cosmological parameter and overdensity values defined in Sec. 3.4 and follow Refs. [33, 73] to model the concentration, generalising this approach beyond the $\omega = 0$ case of $f(R)$ gravity with the computation of the linear matter power spectrum as described in Sec. 3.1. We refer to Sec. 4.2 for more details on the modelling of $c_{\rm vir}$, $\rho_{\rm s}$, and $r_{\rm s}$.

In Fig. 1, we show the Solar System constraints the approximation $\delta\varphi_{\rm lin,0}(r_{\rm cham}) \approx 1 - \bar{\varphi}_0$ implies on $|\bar{\varphi}_0 - 1|$ as a function of ω and α. While the constraints do only depend very weakly on the exponent of the scalar field potential α, they scale with the Brans-Dicke parameter ω

approximately as

$$|\bar{\varphi}_0 - 1| \lesssim \frac{5}{6 + 4\omega} \times 10^{-6}. \tag{2.34}$$

For $f(R)$ gravity, where $\omega = 0$, this implies that $|\bar{f}_{\bar{R}0}| = |\bar{\varphi}_0 - 1| \lesssim 8 \times 10^{-7}$, which is in agreement with Ref. [7].

Note that when neglecting the integration constant in Eq. (2.20), we can also write the constraint in Eq. (2.34) as $|\varphi_0 - 1| \lesssim 2|\Psi_N|/(3 + 2\omega)$. We can furthermore combine the constraint in Eq. (2.34), assuming equality, with the background constraints assumed in Sec. 2.1. The condition that $\bar{U}_0 \approx \Lambda$ implies that

$$\frac{1}{6 + 4\omega} \ll 10^5 \alpha. \tag{2.35}$$

Hence, the modification satisfies $\alpha \gg |\bar{\varphi}_0 - 1|$ assumed in Sec. 2.2 and $|\omega| \ll |\bar{\varphi}_0 - 1|^{-1}$ assumed in Sec. 2.1. Finally, note that, in general, the constraint in Eq. (2.34) does not apply to chameleon fields which couple differently to the baryons than to the dark matter field.

3 Structure formation in the presence of a chameleon field

In the following, we study the formation and evolution of structure in the cold dark matter scenarios of ΛCDM and scalar-tensor gravity given by the action Eq. (2.1) and scalar field potential Eq. (2.13). We first describe the linear growth of structure for ΛCDM models and in the quasistatic regime of scalar-tensor gravity in Sec. 3.1. In Sec. 3.2, we discuss the spherical collapse model for chameleon theories and in Sec. 3.3, we examine the role of the environmental density in this approach. Finally, in Sec. 3.4, we give details on the N-body simulations employed in our study, which we use in Sec. 4 to test the chameleon spherical collapse and halo model predictions.

3.1 Linear growth of structure in scalar-tensor theories

Combining the linearly perturbed Einstein field equations with the energy-momentum conservation in the total matter gauge of ΛCDM yields an ordinary second-order differential equation for the evolution of the matter overdensity $\Delta_{\mathrm{m}}(a, k)$,

$$\Delta_{\mathrm{m}}'' + \left[2 - \frac{3}{2}\Omega_{\mathrm{m}}(a)\right]\Delta_{\mathrm{m}}' - \frac{3}{2}\Omega_{\mathrm{m}}(a)\Delta_{\mathrm{m}} = 0, \tag{3.1}$$

where we have defined $\Omega_{\mathrm{m}}(a) \equiv H_0^2 \Omega_{\mathrm{m}} a^{-3}/H^2$ with the matter energy density parameter Ω_{m} and the Hubble parameter and constant H and H_0, respectively. We replace Δ_{m} in Eq. (3.1) with the linear growth function

$$D(a) \equiv \frac{\Delta_{\mathrm{m}}(a, k)}{\Delta_{\mathrm{m}}(a_{\mathrm{i}}, k)}D(a_{\mathrm{i}}) \tag{3.2}$$

and solve for $D(a)$ assuming matter domination with the corresponding initial conditions $D(a_{\mathrm{i}}) = a_{\mathrm{i}}$ and $D'(a_{\mathrm{i}}) = a_{\mathrm{i}}$ at an initial scale factor $a_{\mathrm{i}} \ll 1$. Here and throughout the paper, $D(a)$ shall refer to the linear growth function of a ΛCDM cosmology.

In scalar-tensor theories, Eq. (3.2) is modified and in the quasistatic limit reads [42, 74, 75]

$$\Delta_{\mathrm{m}}'' + \left[2 - \frac{3}{2}\Omega_{\mathrm{m}}(a)\right]\Delta_{\mathrm{m}}' - \frac{3}{2\bar{\varphi}}\left[1 + \frac{1}{3 + 2\omega}\frac{k^2\bar{\varphi}}{a^2 m^2 + k^2\bar{\varphi}}\right]\Omega_{\mathrm{m}}(a)\Delta_{\mathrm{m}} \simeq 0, \tag{3.3}$$

describing the time and scale dependent linear growth function $D_\varphi(a,k)$ defined as in Eq. (3.2) for scalar-tensor theories. Note that contrary to ΛCDM, at near-horizon scales, the quasistatic $D_\varphi(a,k)$ obtained from solving Eq. (3.3) deviates from the growth of matter fluctuations inferred from solving the full linear cosmological perturbation theory. For the scalar-tensor theories of interest here, however, these deviations are small [25, 42, 76–78] and can safely be neglected in the high-curvature regime studied in the following (cf. [42, 79]). Moreover, we set $\bar{\varphi} \simeq 1$ in Eq. (3.3).

The linear matter power spectrum for the chameleon models $P_{\mathrm{L}\varphi}$ can be determined from rescaling the ΛCDM power spectrum $P_{\mathrm{L}\Lambda\mathrm{CDM}}$,

$$P_{\mathrm{L}\varphi}(a,k) = \left(\frac{D_\varphi(a,k)}{D(a)}\right)^2 P_{\mathrm{L}\Lambda\mathrm{CDM}}(a,k), \tag{3.4}$$

where we assume the same initial conditions for the scalar field models as in ΛCDM (see Sec. 3.4). We define the variance by evolving the initial matter fluctuations according to ΛCDM,

$$S(a,r) \equiv \sigma^2(a,r) = \int \mathrm{d}^3\mathbf{k}\,|\tilde{W}(k\,r)|^2 P_{\mathrm{L}\Lambda\mathrm{CDM}}(a,k) = \frac{D^2(a)}{D^2(a_{\mathrm{i}})}\int \mathrm{d}^3\mathbf{k}\,|\tilde{W}(k\,r)|^2 P_{\mathrm{i}}(a_{\mathrm{i}},k), \tag{3.5}$$

where $\tilde{W}(k\,r)$ is a window function, obtained by the Fourier transform of a top-hat function of radius r, and P_{i} is the initial power spectrum at time a_{i}. We also apply this definition to chameleon models, i.e., using $D(a)$ in the extrapolation of the initial matter power spectrum rather than $D_\varphi(a,k)$. In this case, the variance has to be interpreted as an effective quantity. We discuss the advantages of this approach in Sec. 4.1. Note that we can also write S as a function of the mass $M = 4\pi\,\bar{\rho}_{\mathrm{m}}\,r^3/3$ enclosed by the top-hat function instead of r.

3.2 Chameleon spherical collapse

The formation of clusters can be studied with the spherical collapse model, where the dark matter halo is approximated by a spherically symmetric top-hat overdensity, which is evolved according to the nonlinear continuity and Euler equations from an initial time to the time of its collapse. The chameleon suppression in the spherical collapse calculation can be incorporated in this model following Ref. [65] (cf. [80]), who allow a mass and environment dependent modification of the gravitational force by implementing the thin-shell thickness estimator for the chameleon transition by Ref. [4] described in Sec. 2.4. The chameleon spherical collapse model has also been adapted to $f(R)$ gravity and applied in the description of halo mass functions produced by N-body simulations thereof, yielding good agreement between the two [66]. We generalise this description to chameleon models of the form given by Eqs. (2.1) and (2.13), and in Sec. 4, study its application in the modelling of halo properties.

In the following discussion, we denote the physical radius of the top-hat overdensity at time a by $\zeta(a)$, which at the initial time $a_{\mathrm{i}} \ll 1$ is determined by $\zeta(a_{\mathrm{i}}) = a_{\mathrm{i}}r_{\mathrm{th}}$. Due to the nonlinear evolution of the overdensity, $\zeta(a)$ deviates from this simple linear relation when $a > a_{\mathrm{i}}$, which can be described by defining the dimensionless variable $y \equiv \zeta(a)/ar_{\mathrm{th}}$ with $\tilde{\rho} = \rho_{\mathrm{m}}/\bar{\rho}_{\mathrm{m}} = y^{-3}$ as $\bar{\rho}_{\mathrm{m}}a^3 r_{\mathrm{th}}^3 = \rho_{\mathrm{m}}\zeta^3$ due to conservation of mass enclosed in the overdensity. The evolution of the physical radius of the spherical shell is governed by the equation of motion [65, 66, 73]

$$\frac{\ddot{\zeta}}{\zeta} \simeq -\frac{\kappa^2}{6}\left(\bar{\rho}_{\mathrm{m}} - 2\bar{\rho}_\Lambda\right) - \frac{\kappa^2}{6}\left(1 + \frac{\Delta F}{F_{\mathrm{N}}}\right)\delta\rho_{\mathrm{m}}, \tag{3.6}$$

where dots denote cosmic time derivatives and we use the gravitational force modification $\Delta F/F_N$ given in Eq. (2.27), replacing $\Delta r/r_{\rm th} \to \Delta\zeta/\zeta$. Thus, with $\tilde{\rho}_{\rm in} = y_{\rm h}^{-3}$, we obtain the evolution of $y_{\rm h}$ from solving

$$y_{\rm h}'' + \left[2 - \frac{3}{2}\Omega_{\rm m}(a)\right] y_{\rm h}' + \frac{1}{2}\Omega_{\rm m}(a)\left(1 + \frac{\Delta F}{F_N}\right)\left(y_{\rm h}^{-3} - 1\right) y_{\rm h} = 0 \tag{3.7}$$

with the force enhancement following from Eq. (2.24),

$$\frac{\Delta\zeta}{\zeta} \simeq \frac{(3 + 2\omega)(\bar{\varphi}_0 - 1)\, a^{\frac{4-\alpha}{1-\alpha}}}{3\Omega_{\rm m}(H_0 r_{\rm th})^2} y_{\rm h} \left[\left(\frac{1 + 4\frac{\Omega_\Lambda}{\Omega_{\rm m}}}{y_{\rm h}^{-3} + 4\frac{\Omega_\Lambda}{\Omega_{\rm m}}a^3}\right)^{\frac{1}{1-\alpha}} - \left(\frac{1 + 4\frac{\Omega_\Lambda}{\Omega_{\rm m}}}{y_{\rm env}^{-3} + 4\frac{\Omega_\Lambda}{\Omega_{\rm m}}a^3}\right)^{\frac{1}{1-\alpha}}\right]. \tag{3.8}$$

For the environment $\tilde{\rho}_{\rm out} = y_{\rm env}^{-3}$, we assume a ΛCDM evolution, obtained from Eq. (3.6) in the limit $\Delta\zeta/\zeta \to 0$ or equivalently, $\Delta F \to 0$, which yields

$$y_{\rm env}'' + \left[2 - \frac{3}{2}\Omega_{\rm m}(a)\right] y_{\rm env}' + \frac{1}{2}\Omega_{\rm m}(a)\left(y_{\rm env}^{-3} - 1\right) y_{\rm env} = 0, \tag{3.9}$$

forming a system of differential equations together with Eq. (3.7). We solve this system, setting the initial conditions in the matter-dominated regime,

$$y_{\rm h/env,i} = 1 - \frac{\delta_{\rm h/env,i}}{3}, \qquad y_{\rm h/env,i}' = -\frac{\delta_{\rm h/env,i}}{3}, \tag{3.10}$$

at an initial scale factor $a_{\rm i} \ll 1$. Finally, analogous to the description of the variance in Sec. 3.1, we define an effective linear overdensity for the chameleon theories,

$$\delta_{\rm h/env}(\mathbf{x}; \zeta_{\rm h/env}) \equiv \frac{D(a)}{D(a_{\rm i})}\delta_{\rm h/env,i}, \tag{3.11}$$

extrapolating initial overdensities to time a using the ΛCDM linear growth function $D(a)$, which is obtained from solving Eq. (3.1) with the definition Eq. (3.2). In particular, we use Eq. (3.11) to define the linear collapse density $\delta_{\rm c}$ and the environmental density $\delta_{\rm env}$, corresponding to the effective linear overdensity at the time when Eq. (3.7) produces a singularity given $\delta_{\rm h,i}$ and the associated linear extrapolation of $\delta_{\rm env,i}$, respectively.

3.3 Environmental density distribution

The environmental density $\delta_{\rm env}$ or $\delta_{\rm env,i}$ affects the gravitational force enhancement via Eq. (3.8) and thus, the enhancement in the growth of structure due to this modification. In order to correctly reproduce the halo properties of chameleon theories measured in N-body simulations and to perform consistent tests of the gravitational modifications against observations, we need to incorporate the environmental effects in our modelling. This can be done by either characterising the quantities measured in simulations and from observations by their different environmental densities and comparing this to the according predictions from the spherical collapse model or by studying the averaged observables against the environmentally averaged spherical collapse predictions.

We follow the second approach and define the size of the environments by their Eulerian (physical) radius ζ and therefor adopt the value $\zeta = 5h^{-1}$ Mpc used in Refs. [66, 81]. The
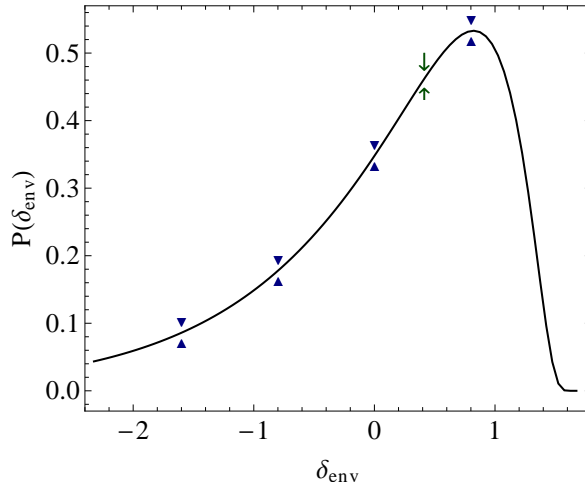
Figure 2. Probability distribution $P(\delta_{\mathrm{env}})$ of the Eulerian environment. The blue diamonds indicate the different environmental densities studied in Sec. 4 and the green arrows mark the environmental density for which the collapse density approximately matches the environmentally averaged counterpart $\langle \delta_{\mathrm{c}} \rangle_{\mathrm{env}}$.

probability distribution of the Eulerian environmental density δ_{env} can approximately be described by [81–83]

$$P_\zeta(\delta_{\mathrm{env}}) = \frac{\beta^{\varpi/2}}{\sqrt{2\pi}} \left[1 + (\varpi - 1)\frac{\delta_{\mathrm{env}}}{\delta_{\mathrm{c}}} \right] \left(1 - \frac{\delta_{\mathrm{env}}}{\delta_{\mathrm{c}}} \right)^{-\varpi/2-1} \exp\left[-\frac{\beta^\varpi}{2} \frac{\delta_{\mathrm{env}}}{(1 - \delta_{\mathrm{env}}/\delta_{\mathrm{c}})^\varpi} \right] \quad (3.12)$$

with $\beta = (\zeta/8)^3/\delta_{\mathrm{c}}/\sigma_8^{2/\varpi}$, $\varpi = \delta_{\mathrm{c}}\gamma$, and

$$\gamma = -\frac{\mathrm{d}\ln S_\xi}{\mathrm{d}\ln M_{\mathrm{env}}} = \frac{\tilde{n}_{\mathrm{s}} + 3}{3}, \quad (3.13)$$

where we assume that the environment evolves according to ΛCDM. Here, ξ is the Lagrangian (or initial comoving) radius with $\xi = 8h^{-1}$ Mpc such that $S_\xi = \sigma_8^2$ and $\tilde{n}_{\mathrm{s}}$ is the slope of the matter power spectrum $P_{\mathrm{L}}(k)$ on large scales at an initial time $a_{\mathrm{i}} \ll 1$ in the matter era after the turn over, corresponding to the initial time used in the excursion set calculation.

We show the distribution $P_\zeta(\delta_{\mathrm{env}})$, assuming cosmological parameter values as defined in Sec. 3.4 in Fig. 2. It can be used to determine the environmentally averaged linear collapse density $\langle \delta_{\mathrm{c}} \rangle_{\mathrm{env}}$, which can then be applied in the modelling of halo properties. We will study this case along with further environmental densities, $\delta_{\mathrm{env}} \simeq 0.8, 0, -0.8, -1.6$, corresponding to the locations of the diamond markers illustrated in Fig. 2. Alternatively and more accurately, observables may first be modelled using $\delta_{\mathrm{c}}(\delta_{\mathrm{env}})$ with subsequent averaging over $P_\zeta(\delta_{\mathrm{env}})$. The two approaches yield only small deviations in the corresponding halo mass functions [66] such that here, for simplicity, we shall use the first method. Note that in two further, very simple, and approximately model-independent approaches, one can approximate the averaged observable by evaluating it at the peak of the environmental distribution $\delta_{\mathrm{env}} \approx 0.8$ or for the average environment $\langle \delta_{\mathrm{env}} \rangle_{\mathrm{env}} \approx 0.16$ instead, for which deviations from using $\langle \delta_{\mathrm{c}} \rangle_{\mathrm{env}} \approx \delta_{\mathrm{c}}(\delta_{\mathrm{env}} = 0.4)$ can be estimated by comparing the results obtained for the different environmental densities shown in Fig. 2.

We refer to Refs. [66, 81, 83] for more details on the role of the environment in determining the chameleon modifications.

3.4 N-body simulations of chameleon $f(R)$ gravity

Finally, N-body simulations are an essential tool for understanding the formation of large-scale structure on nonlinear scales and as such provide a great laboratory for studying the chameleon mechanism. Thus, in order to test the accuracy of our predictions obtained from the chameleon spherical collapse and halo model in Sec. 4, we restrict to cases with $\omega = 0$ and use the large-volume, high-resolution dark matter chameleon $f(R)$ gravity simulation output of Ref. [84]. These simulations are performed using an adaptive particle mesh code [62], which solves the quasistatic modified Poisson and scalar field equations (see, e.g., [59]), and cover the Newtonian and chameleon scenarios for each field strength $|\bar{\varphi}_0 - 1| = |\bar{f}_{\bar{R}0}| = 10^{-6}, 10^{-5}, 10^{-4}$ with exponent $\alpha = 1/2$ ($n = 1$). The cosmological parameters are set to $\Omega_\mathrm{m} = 1 - \Omega_\Lambda$ with $\Omega_\Lambda = 0.76$, $h = 0.73$ for the dimensionless Hubble constant, $n_\mathrm{s} = 0.958$ is the slope of the primordial power spectrum, and the initial power in curvature fluctuations A_s is set to correspond to a power spectrum normalisation $\sigma_8 \equiv \sigma(a = 1, r = 8\ h^{-1}\mathrm{Mpc}) = 0.8$ in ΛCDM. We use a simulation of box size $L_\mathrm{box} = 1.0\ h^{-1}$ Gpc and total particle number $N_\mathrm{p} = 1024^3$. The grid structure efficiently follows the density distribution to better resolve the high-density regions as during the simulation, in regions where the local densities are sufficiently large to reach a predefined threshold, the domain grids are progressively refined. We use a spherical overdensity algorithm [85] to identify halos within the simulation and their associated masses. In the process of defining the halos, we use the virial overdensity $\Delta_\mathrm{vir} \approx 390$, which is obtained assuming ΛCDM. We also apply this value to identify halos produced in scalar-tensor gravity, which allows us to make a fair comparison between the different models based on an equal-overdensity approach. Note that the error of using ΛCDM virial masses M_vir instead of accurate virial masses for the chameleon models is estimated to be small compared to the overall modification from the enhanced force [66]. Furthermore, note that we restrict to quasistatic $f(R)$ gravity N-body simulations, where deviations from relaxing this assumption are expected to be small [59, 64].

4 Chameleon halo modelling

Using the chameleon spherical collapse model described in Sec. 3.2, we model the halo mass function and the linear halo bias in the peak-background split using the Sheth-Tormen prescription [67] in Sec. 4.1. In Sec. 4.2, we then approximate the chameleon halos by NFW profiles and model the characteristic density and scale via the halo concentration, for which we introduce a scaling function based on a fit to ΛCDM N-body simulations. Finally, in Sec. 4.3, we combine these descriptions to approximate the nonlinear matter power spectrum using the halo model.

4.1 Halo mass function and linear halo bias

The statistics of virialised clusters can be described using excursion set theory, where collapsed structures correspond to regions for which the smoothed initial matter density fields exceed the threshold given by the collapse density δ_c. The size of such a region relates to the variance S via the integration of the power spectrum $P_\mathrm{L}(k)$ in Eq. (3.5). If the wavenumbers are uncorrelated, an incremental step in the smoothed initial overdensity field from changing S is independent of its previous values. The smoothed matter density field is then described by a Brownian motion in S with Gaussian probability distribution, for which the increment is a Gaussian field with zero mean. The Press-Schechter [86] expression describes the distribution f of the Brownian motion trajectories that first cross the flat barrier δ_c at S.

For chameleon models, however, due to the scale-dependent modification of gravity, the barrier is no longer flat and depends on S and the environment embedding the collapsing halo. Similarly, if relaxing the assumption of sphericity of the halo, the barrier becomes dependent on S. Motivated by excursion set theory with a moving barrier such as caused by ellipsoidal collapse [87, 88], Sheth and Tormen [67] introduced a modification of the Press-Schechter expression for the first-crossing distribution f given by

$$\nu f(\nu) = \mathcal{N}\sqrt{\frac{2}{\pi}q\,\nu^2}\left[1 + \left(q\,\nu^2\right)^{-p}\right]e^{-q\,\nu^2/2}, \tag{4.1}$$

where $\nu \equiv \delta_c/\sqrt{S}$ is the peak-threshold, $\mathcal{N}$ is a normalisation parameter such that $\int d\nu\, f(\nu) = 1$, $p = 0.3$, and $q = 0.707$ is set to match results from ΛCDM N-body simulations in the halo mass function

$$n_{\ln M_{\mathrm{vir}}} \equiv \frac{dn}{d\ln M_{\mathrm{vir}}} = \frac{\bar{\rho}_m}{M_{\mathrm{vir}}}f(\nu)\frac{d\nu}{d\ln M_{\mathrm{vir}}}. \tag{4.2}$$

Eq. (4.1) has been shown to also provide good fits to N-body simulations of linearised $f(R)$ gravity [73] and chameleon $f(R)$ gravity [66] when using the mass and environment dependent collapse density described in Sec. 3.2. We adopt this approach to model the halo mass function of the scalar-tensor models given by Eqs. (2.1) and (2.13), using the effective linear collapse density δ_c obtained from the chameleon spherical collapse and the effective variance in Eq. (3.5) to determine the chameleon peak-threshold ν (cf. [89, 90]). Note that the effective collapse density δ_c is defined by the extrapolation of the initial overdensity leading to collapse at a using the ΛCDM growth of structure $D(a)$ from Eq. (3.1). Similarly, the variance S in Eq. (3.5) is obtained from the integration of the initial matter power spectrum and extrapolated to a using $D(a)$. Hence, we have $\nu = \delta_c/\sqrt{S} = \delta_{c,i}/\sqrt{S_i} = \nu_i$ due to the scale-independent growth of structure in ΛCDM. In contrast, using $D_\varphi(a, k)$ for the extrapolation of $\delta_{c,i}$ and S_i, we have $\nu \neq \nu_i$ in general. Thus, our definition corresponds to defining the peak-threshold at initial time. We compare the Sheth-Tormen halo mass function using this peak-threshold with N-body simulations of $f(R)$ gravity in Fig. 3, finding good agreement between the two. Note that the halo-finder employed does not identify and remove subhalos from the N-body simulations, which leads to a contamination of the signature at the low-mass end.

The nonlinear dark matter distribution is biased with respect to the linear distribution and in order to determine this bias, on large scales, one can perform a peak-background split. In this approach, short-wavelength modes are regarded as superimposing the long-wavelength modes, perturbing δ_c and modifying the collapse. This perturbation can be expressed via the halo mass function and for the Sheth-Tormen expression Eq. (4.1) yields the linear halo bias [67]

$$b_{\mathrm{L}}(M_{\mathrm{vir}}) \equiv b(k = 0, M_{\mathrm{vir}}) = 1 + \frac{a\,\nu^2 - 1}{\delta_c} + \frac{2p}{\delta_c\left[1 + (a\,\nu^2)^p\right]}. \tag{4.3}$$

In chameleon models, with the relative suppression of the effective linear collapse density δ_c with respect to ΛCDM, b_{L} decreases. Using the spherical collapse model described in Sec. 3.2 to compute δ_c, this modification becomes mass and environment dependent. Note that the halo bias only marginally affects the halo model computation of the power spectrum in Sec. 4.3 through the two-halo term and we do not show it here. We refer the reader to Ref. [73] for a measurement of the linear halo bias from N-body simulations of $f(R)$ gravity.
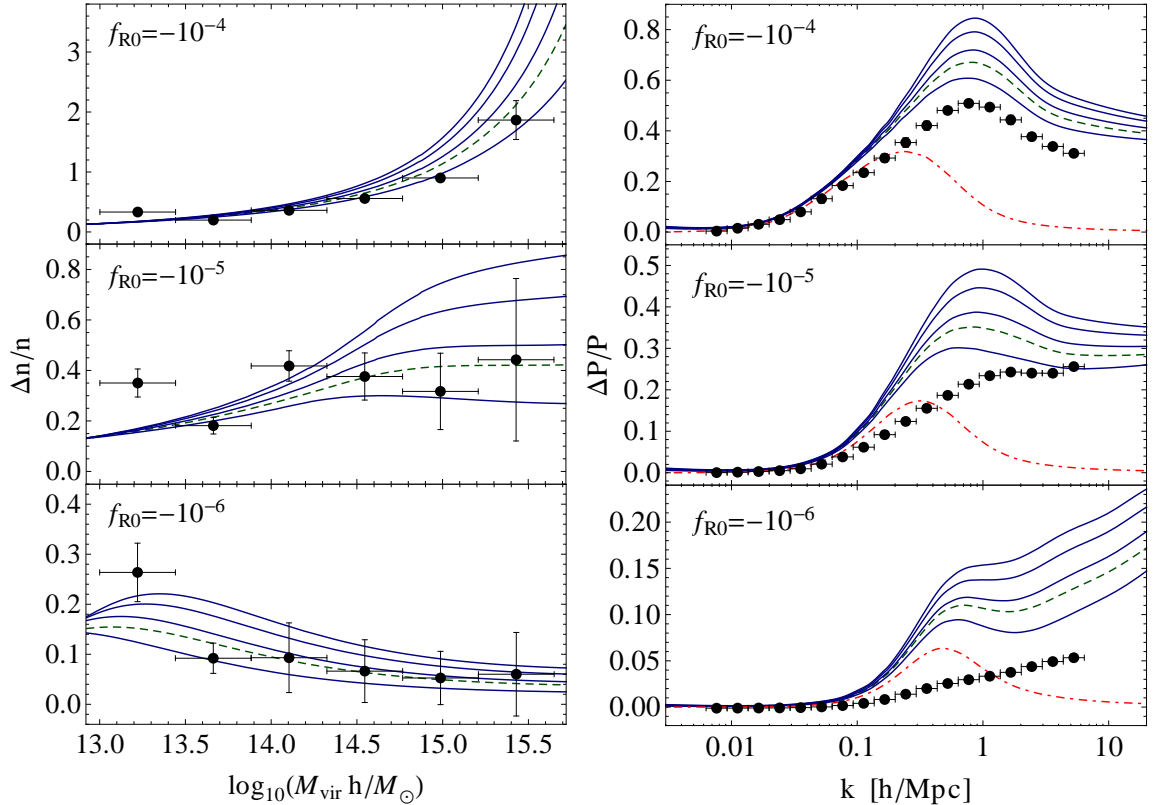
Figure 3. Relative difference between chameleon $f(R)$ and ΛCDM halo mass function $n_{\ln M_{\rm vir}}$ (left panel) and nonlinear matter power spectrum $P(k)$ (right panel) determined from the spherical collapse model, the Sheth-Tormen prescription, the NFW halo profile, and the halo model. The blue solid lines indicate the enhancements obtained for the choices of different environmental densities shown in Fig. 2. The green dashed and red dot-dashed curves correspond to the enhancements obtained from the environmental density $\delta_{\rm env}$ for which $\delta_{\rm c}(\delta_{\rm env}) \approx \langle \delta_{\rm c} \rangle_{\rm env}$ and from adopting halo properties for the $f(R)$ chameleon model that are equivalent to their counterparts from ΛCDM, respectively. We compare our predictions against results from the N-body simulations (data points) of Ref. [84].

4.2 Halo concentration and halo density profiles

In Sec. 2, we have assumed that chameleon halos are spherically symmetric and that their radial density profiles are well described by the NFW fitting function Eq. (2.17). The characteristic density and scale of the NFW fit can be modelled using Eqs. (2.32) and (2.33), respectively, which are functions of the virial mass and concentration, $M_{\rm vir}$ and $c_{\rm vir}$, where we take $\Delta_{\rm vir} = 390$ as in Sec. 3.4. We can reduce this dependency to a function of mass only by adopting a mass-concentration scaling relation such as $c_{\rm vir}(M_{\rm vir}, a) = 9a(M_{\rm vir}/M_*)^{-0.13}$, which has been calibrated to ΛCDM N-body simulations in Ref. [91] using approximately 5×10^3 halos of mass $10^{11} - 10^{14}$ $M_\odot/h$. Hereby, the critical mass M_* satisfies $S(M_*) = \delta_{\rm c}^2$. Note that we assume that the applicability of this calibration can be extended to more massive halos. This scaling relation can further be applied to estimate the concentration of halos formed in scalar-tensor gravity. This approach was taken for $f(R)$ gravity ($\omega = 0$) in Refs. [33, 73, 89], in which M_* is determined by solving $S_\varphi(M_*) = \delta_{\rm c\varphi}^2$, where $\delta_{\rm c\varphi}$ is given by the spherical collapse in the limiting cases of either a $\Delta F/F_{\rm N} = (3 + 2\omega)^{-1}$ or a $\Delta F = 0$ modification and S_φ is the true variance of the scalar-tensor model, i.e., from using $D_\varphi(a, k)$

instead of $D(a)$ in Eq. (3.5). We have followed this approach, generalised to non-zero values of ω, in Sec. 2.5 to obtain a simple estimation for the concentration of the Milky Way halo given its measured mass and derive approximate constraints on the scalar field amplitude $|\bar{\varphi}_0 - 1|$.

As was pointed out in Ref. [56], this approach does, however, not incorporate a chameleon screening effect; M_* is determined from a given scalar field amplitude $(\bar{\varphi}_0 - 1)$ and only introduces a constant shift of the concentration, independent of mass and environment. Here, we evade this deficiency by reinterpreting the mass-concentration relation. We apply the inverse function of the variance to $\sigma(M_*) = \delta_{\rm c}$ to define the critical mass as $M_*(\delta_{\rm c}, \sigma) \equiv \sigma^{-1} \circ \delta_{\rm c}$. This corresponds to assigning an effective flat barrier at each mass and environmental density bin $(M_{{\rm vir},j}, \delta_{{\rm env},k})$ with $\delta_{{\rm c},jk} \equiv \delta_{\rm c}(M_{{\rm vir},j}, \delta_{{\rm env},k})$, interpreting this as a ΛCDM threshold, and performing the standard computation of $M_{*,jk}$ via $\delta_{{\rm c},jk} = \sigma(M_{*,jk})$. Hence, varying $\delta_{\rm c}$ as a function of mass and environment, where σ is determined from the mass, the concentration becomes

$$c_{\rm vir}(M_{\rm vir}, \delta_{\rm env}, a) = 9a \left[\frac{M_*(M_{\rm vir}, \delta_{\rm env})}{M_{\rm vir}} \right]^{0.13}, \tag{4.4}$$

$$M_*(M_{\rm vir}, \delta_{\rm env}) \equiv (\sigma^{-1} \circ \delta_{\rm c})(M_{\rm vir}, \delta_{\rm env}) = \sigma^{-1}(\delta_{\rm c}(M_{\rm vir}, \delta_{\rm env})), \tag{4.5}$$

which introduces a chameleon screening effect in $c_{\rm vir}$.

Given the halo concentration, we can compute the characteristic density $\rho_{\rm s}$ and characteristic radius $r_{\rm s}$ of the NFW profile through Eqs. (2.32) and (2.33). While $\rho_{\rm s}$ is enhanced due to the presence of the chameleon field, $r_{\rm s}$ becomes smaller compared to its ΛCDM counterpart. Thereby, the mass and environmental dependence of the halo concentration is reflected in the modifications of $\rho_{\rm s}$ and $r_{\rm s}$. Note that the halo concentration and, hence, $\rho_{\rm s}$ and $r_{\rm s}$, only marginally affect the halo model computation of the power spectrum in Sec. 4.3 at the smallest scales, mainly through the one-halo term, and we do not show them here. We refer the reader to Ref. [56] for a measurement of the halo concentration, characteristic density, and characteristic radius from N-body simulations of $f(R)$ gravity.

4.3 Nonlinear matter power spectrum

Finally, we use the halo model [92–94] to decompose statistics of cosmological structures into the underlying halo contributions. In this picture, the nonlinear matter power spectrum can be described by the two-halo and one-halo terms,

$$P_{\rm mm}(k) \simeq I^2(k) P_{\rm L}(k) + P^{1h}(k), \tag{4.6}$$

$$P^{1h}(k) = \int {\rm d} \ln M_{\rm vir} n_{\ln M_{\rm vir}} \frac{M_{\rm vir}^2}{\bar{\rho}_{\rm m}^2} |y(k, M_{\rm vir})|^2 \tag{4.7}$$

with

$$I(k) \simeq \int {\rm d} \ln M_{\rm vir} n_{\ln M_{\rm vir}} \frac{M_{\rm vir}}{\bar{\rho}_{\rm m}} y(k, M_{\rm vir}) b_{\rm L}(M_{\rm vir}), \tag{4.8}$$

where $y(k, M)$ shall be the Fourier transform of a NFW density profile which is truncated at $r_{\rm vir}$ and normalised as $\lim_{k \to 0} y(k, M) = 1$. We further require $\lim_{k \to 0} I(k) = 1$. The expressions Eqs. (4.6), (4.7), and (4.8) apply to both ΛCDM and the chameleon model. The halo mass function, halo density profile, and halo bias are computed according to Secs. 4.1 and 4.2. The linear matter power spectrum for ΛCDM and the chameleon model, $P_{\rm L\Lambda CDM}$

and $P_{L\varphi}$ described in Sec. 3.1, respectively, are determined from the initial power spectrum using the Eisenstein-Hu transfer function [95, 96].

We compare the nonlinear matter power spectrum predicted by the halo model in Eq. (4.6) with the power spectrum obtained from N-body simulations for chameleon $f(R)$ gravity in Fig. 3. The blue solid curves illustrate the effects of assuming the different environmental densities of Sec. 3.3 when determining the halo properties used in Eqs. (4.7) and (4.8). They mainly contribute via the one-halo and to a smaller extent through the two-halo contribution. The effect of the environment can be interpreted as an average over unscreened, screened, and partially screened forces between the dark matter particles. The green dashed curve corresponds to the average obtained for the environmental density $\delta_{\rm env}$ for which $\langle \delta_c \rangle_{\delta_{\rm env}} \approx \delta_c(\delta_{\rm env})$ and the red dot-dashed curve represents the case in which $I(k)$ and the one-halo term correspond to the contributions expected in a ΛCDM model, or equivalently, where the halo mass function, halo bias, and halo profile are computed for an extreme high-density environment.

Compared to ΛCDM, in $f(R)$ gravity, nonlinearities contribute at slightly larger scales; whereas for ΛCDM, at $k = 0.1\ h\,{\rm Mpc}^{-1}$, the linear power spectrum is about 5% smaller than its nonlinear counterpart, at the same scale, in $f(R)$ gravity, for $|\bar{f}_{\bar{R}0}| = 10^{-4}$, this deviation is about 10%. For both models, the two-halo term approximately corresponds to the linear power spectrum and only at small scales is suppressed with respect to P_L, i.e., $\gtrsim 5\%$ at $k \gtrsim 1\ h\,{\rm Mpc}^{-1}$. It only marginally affects the interpolation between the linear power spectrum and the one-halo term. In ΛCDM, the one-halo term starts to dominate over the two-halo term at $k \gtrsim (0.4 - 0.5)\ h\,{\rm Mpc}^{-1}$. This scale of equality between the two contributions is slightly shifted to larger scales for $f(R)$ models.

In the left panel of Fig. 4, we show the relative enhancement of the power spectrum of $f(R)$ gravity with respect to ΛCDM predicted by the original [97] and revised [98] HALOFIT approaches. Both descriptions fail to capture the suppression of the small-scale enhancement of the power in the small-field limit. While the revised HALOFIT improves the description of the power spectrum enhancement for $|\bar{f}_{\bar{R}0}| = 10^{-4}$ over the original version, it yields a worse fit to this enhancement in the chameleon screened regime $|\bar{f}_{\bar{R}0}| = 10^{-6}$. In comparison, the halo model provides a good qualitative description of the power spectrum at high k-modes but fails to reproduce the correct amplitude of the modification, particularly at intermediate scales, which are described by the two-halo term. We use the linear power spectrum for the computation of this contribution, which underestimates nonlinear effects on these intermediate scales such as a chameleon suppression of the linearly computed growth enhancement. To account for this deficiency, we introduce a simple interpolation function, replacing the linear power spectrum $P_{L\varphi}(k)$ with

$$P_{L\varphi}^{\rm eff}(a, k) = \frac{P_{L\varphi}(a, k) + (k/k_*)P_{L\Lambda{\rm CDM}}(a, k)}{1 + k/k_*},\tag{4.9}$$

where $k_* = 0.1\sqrt{(1 - \bar{\varphi})/10^{-5}}$, motivated by the relation of scale and scalar field amplitude in Eq. 2.24. For the computation of the one-halo term, we then assume the most probable environmental density, corresponding to the position of the peak of Fig. 2. We show the resulting adjusted halo model prediction for the relative enhancement of the power spectrum in the right panel of Fig. 4, which is in good agreement with the N-body simulations over a wide range of scales.

Note that alternatively to our modified halo model approach, the description of the enhancement in the nonlinear matter power spectrum can be improved by employing fitting
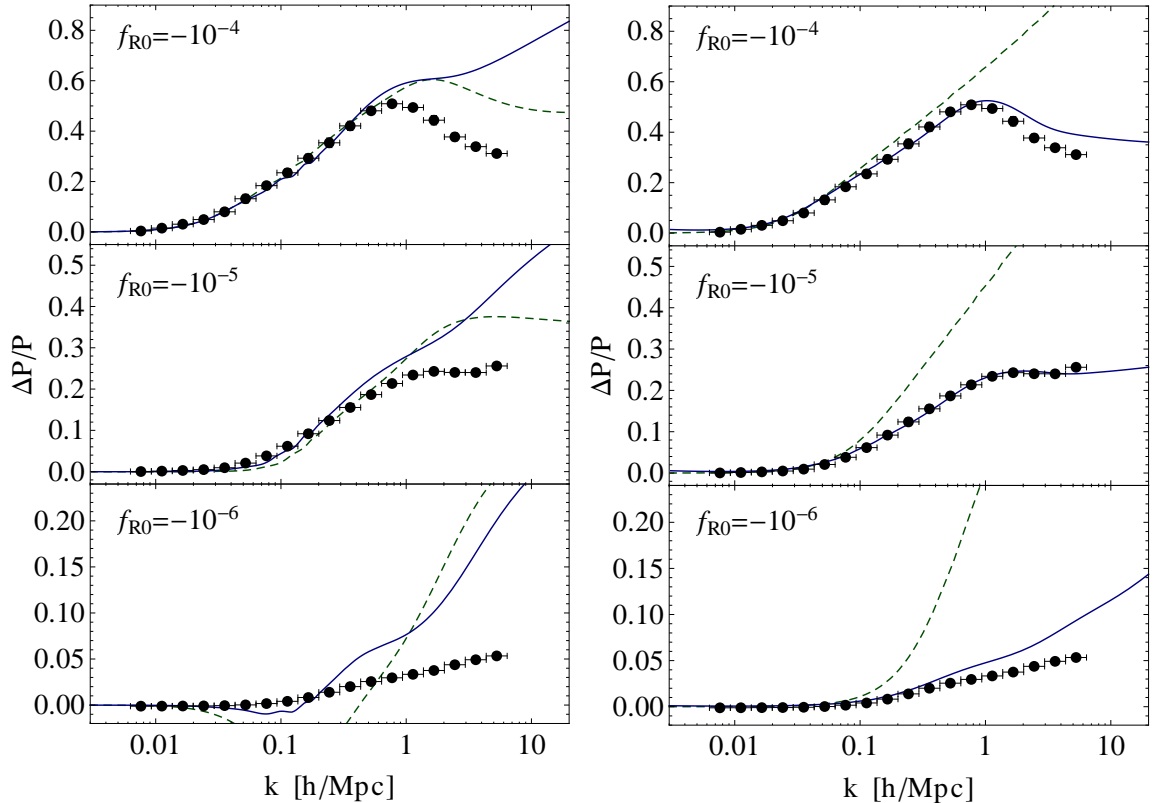
Figure 4. Same as Fig. 3 but for different computations of the matter power spectrum. The different curves show the relative deviations between $f(R)$ and ΛCDM predictions obtained from using: the original [97] (solid blue) and revised [98] (dashed green) HALOFIT approaches in the left panel; the halo model with modified two-halo term (solid blue) and the linear power spectra only (dashed green) in the right panel.

functions as have been devised in Refs. [70, 89, 99, 100], perturbation theory [101], or a combination of the halo model with one-loop perturbations [102].

5   Conclusion

We generalise the Hu-Sawicki $f(R)$ gravity model to scalar-tensor models with constant Brans-Dicke parameter that match a ΛCDM expansion history and undergo chameleon screening of the scalar field and suppression of the gravitational modifications within high-density regions. Based on Solar System constraints on possible deviations from GR, we formulate constraints on the model parameters of our scalar-tensor theories for being locally viable.

We then study the linear and nonlinear large-scale structure produced in our models by implementing the thin-shell estimation of the chameleon force enhancement in the spherical collapse model, which becomes mass and scale dependent in this case. Applying the resulting effective collapse density to the Sheth-Tormen prescription, we determine the halo mass function and linear halo bias of the chameleon models. We furthermore provide simple descriptions of the radial scalar field profile within virialised clusters using the NFW fitting function. Based on the chameleon spherical collapse model, we introduce a mass and environment dependent chameleon modification to a mass-concentration scaling relation that

is calibrated to ΛCDM N-body simulations. This allows us to determine the NFW fitting parameters given the virial mass of the halo and its environmental density. Finally, we use the halo model to describe the nonlinear matter power spectrum using our scalar-tensor modification of the linear matter power spectrum, the Sheth-Tormen halo mass function and linear halo bias, as well as the halo concentration entering the NFW halo profile. We compare the halo model prediction against the nonlinear matter power spectrum extracted from N-body simulations of $f(R)$ gravity; while it provides a good qualitative description of the shape of the enhancement at high k-modes, it fails to recover the correct amplitude. Introducing an effective linear power spectrum in the computation of the two-halo term that interpolates between the linear power spectrum of the chameleon model and ΛCDM and accounts for an underestimation of the chameleon suppression at intermediate scales through the linear approach, we can accurately reproduce the measurements from the N-body simulations over a wide range of scales.

Overall, the modelling procedures for the cosmological observables described in this paper provide useful tools to efficiently extrapolate and interpolate the nonlinear quantities extracted from N-body simulations beyond the simulated values of the cosmological and chameleon model parameters implemented. Approaches of this kind are essential for the consistent study of model constraints from the observed large-scale structure, enabling sufficient and smooth variation of chain parameters as well as statistical convergence.

Acknowledgements

References

[1] J. Wang, L. Hui, and J. Khoury, *No-Go Theorems for Generalized Chameleon Field Theories*, *Phys.Rev.Lett.* **109** (2012) 241301, [arXiv:1208.4612].

[2] C. M. Will, *The confrontation between general relativity and experiment*, *Living Rev. Rel.* **9** (2005) 3, [gr-qc/0510072].

[3] J. Khoury and A. Weltman, *Chameleon fields: Awaiting surprises for tests of gravity in space*, *Phys.Rev.Lett.* **93** (2004) 171104, [astro-ph/0309300].

[4] J. Khoury and A. Weltman, *Chameleon cosmology*, *Phys. Rev.* **D69** (2004) 044026, [astro-ph/0309411].

[5] P. Brax, C. van de Bruck, A.-C. Davis, J. Khoury, and A. Weltman, *Detecting dark energy in orbit - The Cosmological chameleon*, *Phys.Rev.* **D70** (2004) 123518, [astro-ph/0408415].

[6] J. Cembranos, *The Newtonian limit at intermediate energies*, *Phys.Rev.* **D73** (2006) 064029, [gr-qc/0507039].

[7] W. Hu and I. Sawicki, *Models of f(R) Cosmic Acceleration that Evade Solar-System Tests*, *Phys. Rev.* **D76** (2007) 064004, [arXiv:0705.1158].

[8] H. A. Buchdahl, *Non-linear Lagrangians and cosmological theory*, *Mon. Not. Roy. Astron. Soc.* **150** (1970) 1.

[9] A. A. Starobinsky, *Spectrum of relict gravitational radiation and the early state of the universe*, *JETP Lett.* **30** (1979) 682–685.

[10] A. A. Starobinsky, *A new type of isotropic cosmological models without singularity*, *Phys. Lett.* **B91** (1980) 99–102.

[11] S. Capozziello, S. Carloni, and A. Troisi, *Quintessence without scalar fields*, *Recent Res. Dev. Astron. Astrophys.* **1** (2003) 625, [astro-ph/0303041].

[12] S. M. Carroll, V. Duvvuri, M. Trodden, and M. S. Turner, *Is cosmic speed-up due to new gravitational physics?*, *Phys. Rev.* **D70** (2004) 043528, [astro-ph/0306438].

[13] S. Nojiri and S. D. Odintsov, *Modified gravity with negative and positive powers of the curvature: Unification of the inflation and of the cosmic acceleration*, *Phys. Rev.* **D68** (2003) 123512, [hep-th/0307288].

[14] P. Zhang, *Testing f(R) gravity against the large scale structure of the universe.*, *Phys.Rev.* **D73** (2006) 123504, [astro-ph/0511218].

[15] Y.-S. Song, W. Hu, and I. Sawicki, *The large scale structure of f(R) gravity*, *Phys. Rev.* **D75** (2007) 044004, [astro-ph/0610532].

[16] B. Li and J. D. Barrow, *The Cosmology of f(R) gravity in metric variational approach*, *Phys.Rev.* **D75** (2007) 084010, [gr-qc/0701111].

[17] P. Zhang, M. Liguori, R. Bean, and S. Dodelson, *Probing Gravity at Cosmological Scales by Measurements which Test the Relationship between Gravitational Lensing and Matter Overdensity*, *Phys. Rev. Lett.* **99** (2007) 141302, [arXiv:0704.1932].

[18] Y.-S. Song, H. Peiris, and W. Hu, *Cosmological Constraints on f(R) Acceleration Models*, *Phys. Rev.* **D76** (2007) 063517, [arXiv:0706.2399].

[19] B. Jain and P. Zhang, *Observational Tests of Modified Gravity*, *Phys.Rev.* **D78** (2008) 063503, [arXiv:0709.2375].

[20] P. Brax, C. van de Bruck, A.-C. Davis, and D. J. Shaw, *f(R) Gravity and Chameleon Theories*, *Phys. Rev.* **D78** (2008) 104021, [arXiv:0806.3415].

[21] G.-B. Zhao, L. Pogosian, A. Silvestri, and J. Zylberberg, *Searching for modified growth patterns with tomographic surveys*, Phys.Rev. **D79** (2009) 083513, [arXiv:0809.3791].

[22] F. Schmidt, A. Vikhlinin, and W. Hu, *Cluster Constraints on f(R) Gravity*, Phys. Rev. **D80** (2009) 083505, [arXiv:0908.2457].

[23] T. Giannantonio, M. Martinelli, A. Silvestri, and A. Melchiorri, *New constraints on parametrised modified gravity from correlations of the CMB with large scale structure*, JCAP **1004** (2010) 030, [arXiv:0909.2045].

[24] R. Reyes et al., *Confirmation of general relativity on large scales from weak lensing and galaxy velocities*, Nature **464** (2010.) 256–258, [arXiv:1003.2185].

[25] L. Lombriser, A. Slosar, U. Seljak, and W. Hu, *Constraints on f(R) gravity from probing the large-scale structure*, Phys. Rev. **D85** (2012) 124038, [arXiv:1003.3009].

[26] K. Yamamoto, G. Nakamura, G. Hutsi, T. Narikawa, and T. Sato, *Constraint on the cosmological f(R) model from the multipole power spectrum of the SDSS luminous red galaxy sample and prospects for a future redshift survey*, Phys.Rev. **D81** (2010) 103517, [arXiv:1004.3231].

[27] X. Wang, X. Chen, and C. Park, *Topology of large scale structure as test of modified gravity*, Astrophys.J. **747** (2012) 48, [arXiv:1010.3035].

[28] S. Ferraro, F. Schmidt, and W. Hu, *Cluster Abundance in f(R) Gravity Models*, Phys.Rev. **D83** (2011) 063503, [arXiv:1011.0992].

[29] B. Jain and J. VanderPlas, *Tests of Modified Gravity with Dwarf Galaxies*, JCAP **1110** (2011) 032, [arXiv:1106.0065].

[30] A. Hojjati, L. Pogosian, and G.-B. Zhao, *Testing gravity with CAMB and CosmoMC*, JCAP **1108** (2011) 005, [arXiv:1106.4543].

[31] H. Gil-Marin, F. Schmidt, W. Hu, R. Jimenez, and L. Verde, *The Bispectrum of f(R) Cosmologies*, JCAP **1111** (2011) 019, [arXiv:1109.2115].

[32] R. Wojtak, S. H. Hansen, and J. Hjorth, *Gravitational redshift of galaxies in clusters as predicted by general relativity*, Nature **477** (2011) 567–569, [arXiv:1109.6571].

[33] L. Lombriser, F. Schmidt, T. Baldauf, R. Mandelbaum, U. Seljak, et al., *Cluster Density Profiles as a Test of Modified Gravity*, Phys. Rev. **D85** (2012) 102001, [arXiv:1111.2020].

[34] A. Terukina and K. Yamamoto, *Gas density profile in dark matter halo in chameleon cosmology*, Phys.Rev. **D86** (2012) 103503, [arXiv:1203.6163].

[35] E. Di Valentino, A. Melchiorri, V. Salvatelli, and A. Silvestri, *Parametrised modified gravity and the CMB Bispectrum*, Phys.Rev. **D86** (2012) 063517, [arXiv:1204.5352].

[36] B. Jain, V. Vikram, and J. Sakstein, *Astrophysical Tests of Modified Gravity: Constraints from Distance Indicators in the Nearby Universe*, Astrophys.J. **779** (2013) 39, [arXiv:1204.6044].

[37] L. Samushia, B. A. Reid, M. White, W. J. Percival, A. J. Cuesta, et al., *The Clustering of Galaxies in the SDSS-III DR9 Baryon Oscillation Spectroscopic Survey: Testing Deviations from Λ and General Relativity using anisotropic clustering of galaxies*, Mon.Not.Roy.Astron.Soc. **429** (2013) 1514–1528, [arXiv:1206.5309].

[38] J.-h. He, *Testing f(R) dark energy model with the large scale structure*, Phys.Rev. **D86** (2012) 103505, [arXiv:1207.4898].

[39] B. Hu, M. Liguori, N. Bartolo, and S. Matarrese, *Future CMB ISW-Lensing bispectrum constraints on modified gravity in the Parameterized Post-Friedmann formalism*, Phys.Rev. **D88** (2013) 024012, [arXiv:1211.5032].

[40] H. Okada, T. Totani, and S. Tsujikawa, *Constraints on f(R) theory and Galileons from the latest data of galaxy redshift surveys*, Phys.Rev. **D87** (2013) 103002, [arXiv:1208.4681].

[41] A. Hall, C. Bonvin, and A. Challinor, *Testing General Relativity with 21 cm intensity mapping*, Phys.Rev. **D87** (2013) 064026, [arXiv:1212.0728].

[42] L. Lombriser, J. Yoo, and K. Koyama, *Relativistic effects in galaxy clustering in a parametrized post-Friedmann universe*, Phys.Rev. **D87** (2013) 104019, [arXiv:1301.3132].

[43] P. Brax and A.-C. Davis, *Pulsar Constraints on Screened Modified Gravity*, arXiv:1301.5587.

[44] A. Marchini, A. Melchiorri, V. Salvatelli, and L. Pagano, *Constraints on Modified Gravity from ACT and SPT*, Phys.Rev. **D87** (2013) 083527, [arXiv:1302.2593].

[45] A. Abebe, A. de la Cruz-Dombriz, and P. K. S. Dunsby, *Large Scale Structure Constraints for a Class of f(R) Theories of Gravity*, Phys.Rev. **D88** (2013) 044050, [arXiv:1304.3462].

[46] T. Y. Lam, F. Schmidt, T. Nishimichi, and M. Takada, *Modeling the Phase-Space Distribution around Massive Halos*, Phys.Rev. **D88** (2013) 023012, [arXiv:1305.5548].

[47] W. A. Hellwing, B. Li, C. S. Frenk, and S. Cole, *Hierarchical clustering in chameleon f(R) gravity*, Mon. Not. Roy. Astron. Soc. **435** (Nov., 2013) 2806–2821, [arXiv:1305.7486].

[48] A. Upadhye and J. H. Steffen, *Monopole radiation in modified gravity*, arXiv:1306.6113.

[49] A. Marchini and V. Salvatelli, *Updated constraints from the PLANCK experiment on modified gravity*, Phys.Rev. **D88** (2013) 027502, [arXiv:1307.2002].

[50] B. Hu, M. Liguori, N. Bartolo, and S. Matarrese, *Parametrized modified gravity constraints after Planck*, arXiv:1307.5276.

[51] J. Sakstein, *Stellar Oscillations in Modified Gravity*, arXiv:1309.0495.

[52] Y. Zu, D. Weinberg, E. Jennings, B. Li, and M. Wyman, *Galaxy Infall Kinematics as a Test of Modified Gravity*, arXiv:1310.6768.

[53] Y.-C. Cai, B. Li, S. Cole, C. S. Frenk, and M. Neyrinck, *The Integrated Sachs-Wolfe effect in f(R) gravity*, arXiv:1310.6986.

[54] M. Baldi, F. Villaescusa-Navarro, M. Viel, E. Puchwein, V. Springel, et al., *Cosmic Degeneracies I: Joint N-body Simulations of Modified Gravity and Massive Neutrinos*, arXiv:1311.2588.

[55] **Heidelberg Institute for Theoretical Studies** Collaboration, *Scaling relations and mass bias in hydrodynamical f(R) gravity simulations of galaxy clusters*, arXiv:1311.5560.

[56] L. Lombriser, K. Koyama, G.-B. Zhao, and B. Li, *Chameleon f(R) gravity in the virialized cluster*, Phys. Rev. **D85** (2012) 124054, [arXiv:1203.5125].

[57] A. L. Erickcek, N. Barnaby, C. Burrage, and Z. Huang, *Catastrophic Consequences of Kicking the Chameleon*, Phys. Rev. Lett. **110:171101** (2013) [arXiv:1304.0009].

[58] A. L. Erickcek, N. Barnaby, C. Burrage, and Z. Huang, *Chameleons in the Early Universe: Kicks, Rebounds, and Particle Production*, arXiv:1310.5149.

[59] H. Oyaizu, *Non-linear evolution of f(R) cosmologies I: methodology*, Phys. Rev. **D78** (2008) 123523, [arXiv:0807.2449].

[60] B. Li and H. Zhao, *Structure Formation by Fifth Force I: N-Body vs. Linear Simulations*, Phys.Rev. **D80** (2009) 044027, [arXiv:0906.3880].

[61] B. Li, D. F. Mota, and J. D. Barrow, *N-body Simulations for Extended Quintessence Models*, Astrophys.J. **728** (2011) 109, [arXiv:1009.1400].

[62] B. Li, G.-B. Zhao, R. Teyssier, and K. Koyama, *ECOSMOG: An Efficient Code for Simulating Modified Gravity*, JCAP **1201** (2012) 051, [arXiv:1110.1379].

[63] E. Puchwein, M. Baldi, and V. Springel, *Modified-Gravity-GADGET: a new code for cosmological hydrodynamical simulations of modified gravity models*, Mon. Not. Roy. Astron. Soc. **436** (Nov., 2013) 348–360, [arXiv:1305.2418].

[64] C. Llinares, D. F. Mota, and H. A. Winther, *ISIS: a new N-body cosmological code with scalar fields based on RAMSES*, arXiv:1307.6748.

[65] B. Li and G. Efstathiou, *An Extended Excursion Set Approach to Structure Formation in Chameleon Models*, Mon. Not. Roy. Astron. Soc. **421** (2012) 1431, [arXiv:1110.6440].

[66] L. Lombriser, B. Li, K. Koyama, and G.-B. Zhao, *Modeling halo mass functions in chameleon f(R) gravity*, Phys. Rev. D 87, **123511** (2013) [arXiv:1304.6395].

[67] R. K. Sheth and G. Tormen, *Large scale bias and the peak background split*, Mon. Not. Roy. Astron. Soc. **308** (1999) 119, [astro-ph/9901122].

[68] J. F. Navarro, C. S. Frenk, and S. D. M. White, *The Structure of Cold Dark Matter Halos*, Astrophys. J. **462** (1996) 563–575, [astro-ph/9508025].

[69] C. H. Brans and R. H. Dicke, *Mach's Principle and a Relativistic Theory of Gravitation*, Phys.Rev. **124** (1961) 925.

[70] G.-B. Zhao, B. Li, and K. Koyama, *N-body Simulations for f(R) Gravity using a Self-adaptive Particle-Mesh Code*, Phys. Rev. **D83** (2011) 044007, [arXiv:1011.1257].

[71] R. Pourhasan, N. Afshordi, R. Mann, and A. Davis, *Chameleon Gravity, Electrostatics, and Kinematics in the Outer Galaxy*, JCAP **1112** (2011) 005, [arXiv:1109.0538].

[72] P. J. McMillan, *Mass models of the Milky Way*, Mon.Not.Roy.Astron.Soc. **414** (2011) 2446–2457, [arXiv:1102.4340].

[73] F. Schmidt, M. V. Lima, H. Oyaizu, and W. Hu, *Non-linear Evolution of f(R) Cosmologies III: Halo Statistics*, Phys. Rev. **D79** (2009) 083518, [arXiv:0812.0545].

[74] G. Esposito-Farese and D. Polarski, *Scalar tensor gravity in an accelerating universe*, Phys.Rev. **D63** (2001) 063504, [gr-qc/0009034].

[75] S. Tsujikawa, K. Uddin, S. Mizuno, R. Tavakol, and J. Yokoyama, *Constraints on scalar-tensor models of dark energy from observational and local gravity tests*, Phys.Rev. **D77** (2008) 103009, [arXiv:0803.1106].

[76] A. Hojjati, L. Pogosian, A. Silvestri, and S. Talbot, *Practical solutions for perturbed f(R) gravity*, Phys.Rev. **D86** (2012) 123503, [arXiv:1210.6880].

[77] N. A. Lima and A. R. Liddle, *Linear perturbations in viable f(R) theories*, Phys. Rev. D 88, **043521** (2013) [arXiv:1307.1613].

[78] J. Noller, F. von Braun-Bates, and P. G. Ferreira, *Relativistic scalar fields and the quasi-static approximation in theories of modified gravity*, arXiv:1310.3266.

[79] L. Lombriser, *Consistency check of ΛCDM phenomenology*, Phys. Rev. **D83** (2011) 063519, [arXiv:1101.0594].

[80] A. Borisov, B. Jain, and P. Zhang, *Spherical Collapse in f(R) Gravity*, Phys.Rev. **D85** (2012) 063518, [arXiv:1102.4839].

[81] B. Li and T. Y. Lam, *Excursion set theory for modified gravity: Eulerian versus Lagrangian environments*, Mon. Not. Roy. Astron. Soc. **425** (Sept., 2012) 730–739, [arXiv:1205.0058].

[82] T. Y. Lam and R. K. Sheth, *Perturbation theory and excursion set estimates of the probability distribution function of dark matter, and a method for reconstructing the initial distribution function*, Mon. Not. Roy. Astron. Soc. **386** (May, 2008) 407–415, [arXiv:0711.5029].

[83] T. Y. Lam and B. Li, *Excursion set theory for modified gravity: correlated steps, mass functions and halo bias*, Mon. Not. Roy. Astron. Soc. **426** (Nov., 2012) 3260–3270, [arXiv:1205.0059].

[84] B. Li, W. A. Hellwing, K. Koyama, G.-B. Zhao, E. Jennings, et al., *The nonlinear matter and velocity power spectra in f(R) gravity*, Mon.Not.Roy.Astron.Soc. **428** (2013) 743–755, [arXiv:1206.4317].

[85] A. Jenkins et al., *Mass function of dark matter halos*, Mon. Not. Roy. Astron. Soc. **321** (2001) 372, [astro-ph/0005260].

[86] W. H. Press and P. Schechter, *Formation of Galaxies and Clusters of Galaxies by Self-Similar Gravitational Condensation*, Astrophys. J. **187** (Feb., 1974) 425–438.

[87] R. K. Sheth, H. Mo, and G. Tormen, *Ellipsoidal collapse and an improved model for the number and spatial distribution of dark matter haloes*, Mon. Not. Roy. Astron. Soc. **323** (2001) 1, [astro-ph/9907024].

[88] R. K. Sheth and G. Tormen, *An Excursion set model of hierarchical clustering : Ellipsoidal collapse and the moving barrier*, Mon. Not. Roy. Astron. Soc. **329** (2002) 61, [astro-ph/0105113].

[89] Y. Li and W. Hu, *Chameleon Halo Modeling in f(R) Gravity*, Phys.Rev. **D84** (2011) 084033, [arXiv:1107.5120].

[90] M. Kopp, S. A. Appleby, I. Achitouv, and J. Weller, *Spherical collapse and halo mass function in f(R) theories*, Phys.Rev. **D88** (2013) 084015, [arXiv:1306.3233].

[91] J. S. Bullock, T. S. Kolatt, Y. Sigad, R. S. Somerville, A. V. Kravtsov, et al., *Profiles of dark haloes. Evolution, scatter, and environment*, Mon. Not. Roy. Astron. Soc. **321** (2001) 559–575, [astro-ph/9908159].

[92] J. Peacock and R. Smith, *Halo occupation numbers and galaxy bias*, Mon.Not.Roy.Astron.Soc. **318** (2000) 1144, [astro-ph/0005010].

[93] U. Seljak, *Analytic model for galaxy and dark matter clustering*, Mon.Not.Roy.Astron.Soc. **318** (2000) 203, [astro-ph/0001493].

[94] A. Cooray and R. K. Sheth, *Halo models of large scale structure*, Phys. Rept. **372** (2002) 1–129, [astro-ph/0206508].

[95] D. J. Eisenstein and W. Hu, *Baryonic features in the matter transfer function*, Astrophys.J. **496** (1998) 605, [astro-ph/9709112].

[96] D. J. Eisenstein and W. Hu, *Power spectra for cold dark matter and its variants*, Astrophys.J. **511** (1997) 5, [astro-ph/9710252].

[97] **Virgo Consortium** Collaboration, R. Smith et al., *Stable clustering, the halo model and nonlinear cosmological power spectra*, Mon.Not.Roy.Astron.Soc. **341** (2003) 1311, [astro-ph/0207664].

[98] R. Takahashi, M. Sato, T. Nishimichi, A. Taruya, and M. Oguri, *Revising the Halofit Model for the Nonlinear Matter Power Spectrum*, Astrophys.J. **761** (2012) 152, [arXiv:1208.2701].

[99] W. Hu and I. Sawicki, *A Parameterized Post-Friedmann Framework for Modified Gravity*, Phys. Rev. **D76** (2007) 104043, [arXiv:0708.1190].

[100] G.-B. Zhao arXiv:1312.xxxx.

[101] K. Koyama, A. Taruya, and T. Hiramatsu, *Non-linear Evolution of Matter Power Spectrum in Modified Theory of Gravity*, Phys.Rev. **D79** (2009) 123512, [arXiv:0902.0618].

[102] P. Brax and P. Valageas, *Impact on the power spectrum of screening in modified gravity scenarios*, Phys.Rev. **88** (July, 2013) 023527, [arXiv:1305.5647].